photonics

MDPI

Article

Investigation of Oceanic Turbulence Random Phase Screen Generation Methods for UWOC

Ruixian Jiang [1], Kexin Wang [1], Xinke Tang [2,*] and Xu Wang [1,*]

[1] School of Engineering and Physical Sciences, Heriot-Watt University, Edinburgh EH14 4AS, UK; rj44@hw.ac.uk (R.J.); k.wang@hw.ac.uk (K.W.)
[2] Peng Cheng Laboratory, Shenzhen 518055, China
* Correspondence: tangxk@pcl.ac.cn (X.T.); x.wang@hw.ac.uk (X.W.)

Abstract: Underwater wireless optical communication (UWOC) has recently gained great research interest due to its capability of transmitting data underwater with high data rate and low latency. However, oceanic turbulence seriously degrades the optical signal quality and hence the performance of practical UWOC systems. Establishing more accurate and efficient phase screen models is in demand for studying the oceanic turbulence effect. In this paper, techniques for generating underwater random phase screens are studied and supplemented. A promising hybrid method combining sparse spectrum and Zernike polynomials methods is proposed and investigated, which generates phase screens with improved accuracy and efficiency.

Keywords: underwater wireless optical communication; oceanic turbulence; the random phase screens model; hybrid phase screen

Citation: Jiang, R.; Wang, K.; Tang, X.; Wang, X. Investigation of Oceanic Turbulence Random Phase Screen Generation Methods for UWOC. *Photonics* **2023**, *10*, 832. https://doi.org/10.3390/photonics10070832

Received: 24 May 2023
Revised: 1 July 2023
Accepted: 12 July 2023
Published: 18 July 2023

1. Introduction

In recent years, with growing human activities in the ocean, underwater wireless communication (UWC) technology enabling wireless data transmission between underwater vehicles, devices and sensor nodes has attracted worldwide attention [1–4]. UWC technologies have great potential in ocean exploration and marine environmental monitoring, including monitoring of the Earth's environment in order to tackle the Earth's degradation and environmental destruction [2], as well as the exploration of oil and gas resources and extraction of natural resources [3]. Currently, UWC mainly uses acoustic waves as a physical carrier and has the advantage of long transmission distance [1]. However, underwater acoustic communication has a very narrow bandwidth [4–6]. In contrast, underwater wireless optical communication (UWOC) technology offers high-speed data transmission within short ranges [1]. It also presents great advantages of small size, low latency and high security performance [7,8]. Since Duntley et al. [9] found that relatively low attenuation makes blue–green light suitable as the information carrier for underwater optical communication, UWOC technology has been widely studied and demonstrated [10–14].

However, the performance of practical UWOC systems can be seriously impacted by oceanic turbulence, which was commonly ignored before but has been increasingly studied in recent years. In theory, this effect refers to the random changes of refractive index caused by the gradient of seawater temperature and salinity, which results in scintillation of the light intensity at the receiver [15–20]. In general, the methods for studying light propagation in turbulent media can be broadly classified into three categories: theoretical analysis, numerical simulation and experimental methods [21]. Numerical simulation has been widely used to simulate the effect of turbulence because of its superior simulation efficiency, controllability of turbulence parameters and the acquisition of statistical results [22–24]. As a widely employed approach in the numerical simulation, the phase screen is a programmable high-resolution method which can effectively simulate the impact of turbulence on intensity and phase of the propagating light [25]. This result would also significantly contribute to underwater coherent optical wireless communication systems [26]. Phase screen models can provide an essential reference for experimental investigations on atmospheric and underwater turbulence [27–29] by analyzing the optical characteristics of the turbulence channels. At present, the existing numerical simulation of oceanic turbulence is mainly based on phase screen models with the power spectrum inversion method [30] or the Zernike polynomials method [31]. However, these methods have various shortcomings, such as the absence of low-frequency or high-frequency turbulence components, resulting in inaccurate simulation results and unsatisfactory simulation efficiency [32]. As a solution, the hybrid phase screens technique has also been proposed and demonstrated to simulate both atmospheric and ocean turbulence, which linearly combines the phase screens generated by the power spectrum inversion method and by the Zernike polynomials method [25,31,32]. However, there is a lack of comprehensive study of the hybrid phase screen methods and current methods involve only a limited variety of phase screen generation techniques.

In this paper, the generation methods of random phase screens are comprehensively studied and analyzed for the numerical simulation of oceanic turbulence. The optimal method for generating hybrid phase screens is proposed and validated in a simulation of beam propagation in oceanic turbulence. The rest of the paper is organized as follows: Section 2 gives the principles of phase screen generation methods for the numerical simulation of oceanic turbulence, which provides motivation for the study of new methods. In Section 3, performances of different random phase screen models are comprehensively studied, and the optimal method for generating effective hybrid phase screens is investigated. Finally, a brief conclusion of this paper is drawn in Section 4.

2. Phase Screen Model

The turbulence effect leading to phenomena such as phase drift and light intensity flicker occurs on the receiving plane of the propagated beam, and it can be simulated as a series of phase screens that randomly change the wavefront phase of the beam by numerical simulation [33]. The method is called the random phase screens model [34–36] and it has been widely used for the simulation of atmospheric turbulence [37].

Figure 1 illustrates the random phase screens model of beam propagation in oceanic turbulent environment. These n phase screens are uniformly placed at $z_1, z_2 = z_1 + \Delta z, z_3 = z_1 + 2 \times \Delta z \ldots z_n = z_1 + (n-1) \times \Delta z$ along the propagation direction with a total length of z. Based on the split-step method, the phase perturbation of propagation caused by the turbulence effect can be processed separately by discrete steps along the direction of beam propagation [22,38]. At each discrete step size, random phase perturbations are achieved by multiplying the field of the arriving beam with the phase screen determined by the refractive index fluctuation equation. The phase of the beam is randomly affected when it passes through individual phase screens until it finally reaches the receiving plane [22]. Combining each of these steps completes the representation of beam propagation in turbulence. Various methods have been reported to generate phase screens for studying the effect of turbulence, which can generally be summarized as Frequency Spectrum Method (FSM) and Spatial Domain Method (SDM) [39]. Interestingly, turbulence phase screens can be also generated based on the use of both FSM and SDM, which has been introduced in [31,32].

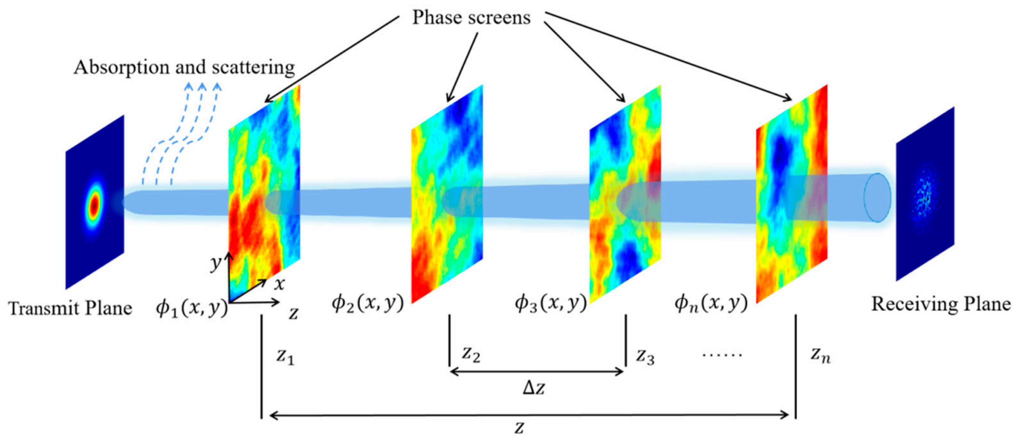

Figure 1. Random phase screens model for beam propagation in an oceanic turbulent environment. Phase screens are respectively represented by ϕ_1, ϕ_2, $\phi_3 \ldots \phi_n$, where $n = 1, 2, 3 \ldots\ldots$ in the x–y plane along the z axis.

2.1. FSMs for Oceanic Turbulence Phase Screen Generation

The FSM generates phase screens by obtaining phase distribution via the turbulence power spectral density function and converting it from the frequency domain to the spatial domain. Different methods focus on different aspects of the phase screen, including spectral components, amplitude and wave vectors. Among these, the power spectrum inversion method (also known as DFT here since it is characterized by discrete Fourier transform) [40,41], sparse spectrum method (SS) [42–44], Paulson, Wu and Davis' method (PWD) [45] and sparse uniform method (SU) [41] are commonly used.

Although these methods have been deeply studied in the random phase screen generation of atmospheric turbulence by using an atmospheric spectrum, only the DFT method has currently been applied to generate oceanic turbulence phase screens [30,46], using the spectrum of turbulent fluctuations of the seawater refraction index, the phase structure function (PSF) and spatial coherence radius of light in oceanic turbulence [47,48].

The fluctuation spectrum of ocean refractive index proposed by Nikishov et al. [47] is given in Equation (1), based on the research about the influence of temperature and salinity on the refractive index of seawater [49] and the variation range of thermal diffusivity of salinity [50,51].

$$\begin{aligned}\Phi(k_x, k_y) = 0.388 \times 10^{-8} \varepsilon^{-1/3} \left(\sqrt{k_x^2 + k_y^2}\right)^{-11/3} \left[1 + 2.35\left(\sqrt{k_x^2 + k_y^2}\,\eta\right)^{2/3}\right] \\ \times \frac{\chi_T}{\omega^2}\left(\omega^2 e^{-A_T\delta} + e^{-A_S\delta} - 2\omega e^{-A_{TS}\delta}\right)\end{aligned} \tag{1}$$

In the equation, Φ is the underwater turbulence refractive index power spectrum density (PSD) and k_x, k_y are the frequency components of the x-axis and y-axis in the spatial frequency domain, respectively. Where ε represents the dynamic dissipation rate per unit volume of seawater ranging from 10^{-10} m^2/s^3 to 10^{-1} m^2/s^3, χ_T is the dissipation rate of the mean squared temperature ranging from 10^{-10} K^2/s to 10^{-4} K^2/s, ω ranging from -5 to 0 is the ratio of the temperature and the salinity contribution to the refractive index spectrum and η is the Kolmogorov microscale length in the order of millimeters for ocean turbulence. In addition, other parameters are given as: $A_T = 1.863 \times 10^{-2}$, $A_S = 1.9 \times 10^{-4}$, $A_{TS} = 9.41 \times 10^{-3}$ and $\delta = 8.234\left(\eta\sqrt{k_x^2 + k_y^2}\right)^{4/3} + 12.978\left(\eta\sqrt{k_x^2 + k_y^2}\right)^2$ [46].

Inspired by this, this paper proposes ocean turbulence phase screen models based on SS, PWD and SU methods by substituting the atmospheric fluctuation spectrum with the fluctuation spectrum of ocean refractive index (Equation (1)). With the PSF of oceanic turbulence in [48], the proposed models are verified and compared. This also offers more candidates for studying the hybrid phase screens in the following sections.

2.2. SDM for Oceanic Turbulence Phase Screen Generation

For spatial domain methods, the turbulence characteristics are calculated directly in the spatial domain. The Zernike polynomials method is a commonly used SDM [32,52], which generates phase screens with a PSF consistent with the theoretical values in the low spatial frequency components [25]. Noll [53] proposed the principle for directly obtaining the distorted wavefront of turbulence by using a complete set of orthonormal functions, such as Zernike polynomials, with which Roddier [31,54] generated an atmospheric turbulent phase screen.

This method is based on combining multiple Zernike modes with their coefficients. Considering the definition given by Noll, the jth order of the Zernike polynomial composed of radial polynomials and angular polynomials is expressed as [53]:

$$Z_j(r) = Z_n^m(r,\theta) = \sqrt{n+1}R_n^m(r)\Theta^m(\theta) \tag{2}$$

where r is a two-dimensional polar vector representing the radial distance, m and n are non-negative integers that correspond to the number of orders j. n is the radial degree and m the azimuthal degree. The radial polynomial $R_n^m(r)$ and angular polynomial $\Theta^m(\theta)$ are given as [53] where k is the nature number, $k = \{0,1,2,3,\ldots\} \in \mathbb{N}$:

$$R_n^m(r) = \begin{cases} \sum_{s=0}^{(n-m)/2} \frac{(-1)^S(n-s)!}{s!\left[\frac{(n+m)}{2}-s\right]!\left[\frac{(n-m)}{2}-s\right]!} r^{n-2s} & , n-m = 2k \\ 0 & , n-m = 2k+1 \end{cases} \tag{3}$$

$$\Theta^m(\theta) = \begin{cases} \sqrt{2}cos(m\theta) & m \neq 0,\ j = 2k \\ \sqrt{2}sin(m\theta) & m \neq 0, j = 2k+1 \\ 1 & m = 0 \end{cases} \tag{4}$$

Thus, the linear combination of two orthogonal Zernike polynomials can represent the phase aberration in any direction. With the increase of the order, the description of the phase aberration becomes more complex, which means the high-frequency components begin to increase. Therefore, phase screens can be represented by linear combination of a series of Zernike polynomials [53]:

$$\phi(r) = \sum_{j=1}^{\infty} a_j Z_j(r) \tag{5}$$

where $\phi(r)$ represents the Zernike phase screen. As the coefficient of the jth order Zernike polynomial, a_j can be obtained by calculating its covariance matrix due to its correlation. The ensemble average of any two coefficients a_j, a_j' can be obtained by calculating the phase structure function, which is defined as follows [53]:

$$D_\varphi(r,r') = \left\langle \left|\varphi(r) - \varphi(r')\right|^2 \right\rangle = 2\left[R_\varphi(0) - R_\varphi(\left|r-r'\right|)\right] \tag{6}$$

where $R_\varphi(|r-r'|)$ is equal to the ensemble average of phase difference between two points on phase screens. For oceanic turbulence, the covariance matrix can be derived by substituting in the PSF of underwater turbulence. The (i,j) element in the covariance matrix can be written as [55]:

$$\langle a_i a_j \rangle = 0.15(D/r_0)^{\frac{5}{3}} \cdot \frac{(-1)^{\frac{n_i+n_j-2m_i}{2}}\left[(n_i+1)(n_j+1)\right]^{\frac{1}{2}}\Gamma(\frac{14}{3})\Gamma\left[(n_i+n_j-\frac{5}{3})/2\right]\delta_{m_i m_j}}{\Gamma(\frac{n_i-n_j+17/3}{2})\Gamma(\frac{n_j-n_i+17/3}{2})\Gamma(\frac{n_i+n_j+23/3}{2})}, \quad i-j = 2k \tag{7}$$

where $\delta_{m_i m_j}$ is the Kronecker function. In addition, n_i n_j, m_i m_j are the Noll coefficients corresponding to the i,jth order of Zernike polynomials, D is the aperture size of the spatial domain and r_0 is the underwater coherence length. Finally, singular value decomposition

(SVD) is applied to the covariance matrix, and the coefficient a_j can be calculated by introducing Gaussian random vector b according to the property of its eigenvector U. Then, by substituting a_j into Equation (8), the phase screen expression can be obtained as:

$$\phi(r) = \sum_{j=1}^{\infty} a_j Z_j(r) = \sum_{j=1}^{\infty} \sum_{k=1}^{\infty} U_{jk} b_j Z_j(r) \tag{8}$$

In simulation, Zernike polynomials for each mode are calculated and the resulting polynomials are added together to generate the final phase screen. By adjusting the order of the Zernike modes used for the phase screen, various oceanic conditions can be simulated. However, although the Zernike method has better performance at a low spatial frequency, it has the disadvantage of insufficient components at a high spatial frequency [25,56].

2.3. Hybrid Methods for Ocean Turbulence Phase Screen Generation

Based on the power spectrum inversion method and Zernike polynomials method, hybrid phase screens have been proposed [32,55]. Specifically, the phase screens generated by these two methods are linearly superposed to obtain hybrid phase screens. Such a hybrid phase screen has been proved to perform better for simulating turbulence with higher computational efficiency [25,32]. For comparison, the pros and cons of FSM, SDM and hybrid methods are summarized in Table 1 below, where these conclusions are verified by our simulation work in the following sections.

Table 1. Comparison of different phase screen generation methods.

	Benefits	Limitations
FSM	• Higher computational efficiency • Generate phase screens with sufficient high-frequency components [25]	• Generate phase screens with insufficient low-frequency components [25] • Research on the simulation of underwater turbulence is limited
SDM (Zernike)	• Generate phase screens with sufficient low-frequency components [25] • The increased order improves accuracy	• Generate phase screens with insufficient high-frequency components [32] • The computational efficiency decreases with increasing order
Hybrid methods	• Relatively high computational efficiency • Generate phase screens with higher accuracy [32]	• Research on the simulation of underwater turbulence is very limited

Combining FSM and SDM is expected to compensate for each other's deficiencies. Thus, a hybrid phase screen can be expressed as: $\varphi_h = a \times \varphi_{FSM} + \varphi_{SDM}$, where the different superposition coefficients a are determined by iteratively updating the PSF to obtain the lowest difference to the theoretical results. φ_h represents the hybrid phase screen and φ_{FSM}, φ_{SDM} represent phase screens generated by FSM and SDM respectively. The superposition coefficient of the phase screen generated by SDM is normalized, so only the superposition coefficients of the phase screen generated by FSM are considered.

In this work, based on the comprehensive investigation of FSMs for oceanic turbulence phase screen generation, four hybrid methods are studied, described herein as DFT + Zernike hybrid method, SS + Zernike hybrid method, PWD + Zernike hybrid method and SU + Zernike hybrid method.

3. Results and Discussion

3.1. Ocean Turbulence Phase Screens Generated by FSM

Using the oceanic turbulence refractive index spectrum illustrated in Equation (1), we apply SS, PWD and SU methods to underwater environment and generate the oceanic turbulence phase screens. PSF can be used as a criterion to verify the simulated phase screen [46]. According to the coherence length r_0 of ocean turbulence [41,48], the theoretical value of the PSF of oceanic turbulence $D(r)$ can be obtained as follows [46,48]:

$$D(r) = 2(r/r_0)^{5/3} \tag{9}$$

where r is a variable in two-dimensional coordinates, representing the distance between any two points in the phase screen. The PSF of the generated phase screens obtained by the simulation is defined as [46]:

$$D(r) = \langle [\phi(\rho + r) - \phi(\rho)]^2 \rangle \tag{10}$$

where ρ is a two-dimensional coordinate, which represents a position on the phase screen and r is distance. The equation represents the average mean square of the phase difference between any two points on the phase screen.

Figure 2 shows the phase screens and phase structure functions (PSFs) obtained by the four FSMs, respectively. The PSF results presented in Figure 2 are mean values obtained from 2000 randomly generated phase screens. The distance represented by r is the distance between two points on phase screens. The small value of r on the axis represents the PSF for the high frequency component, and the large value of r represents the PSF for the low frequency component. The r, as a spatial distance, is inversely proportional to the frequency. Thus, the region having small r corresponds to the high frequency component of the phase screen. In our simulation, the maximum value of r is the radius of the inscribed circle of the phase screen, which is denoted as R. The maximum r is scaled to 1 using the normalization factor R in the calculation of PSFs for simplification. For DFT and PWD methods, they can be combined with subharmonic compensation (SH) techniques to improve the insufficiency in the large-scale phase structure of phase screens because there is no sample near zero region of the power spectrum [41,46,57]. On the other hand, SS and SU methods require no SH compensation because they can produce unbiased non-periodic samples [41].

From Figure 2, the PSFs obtained by DFT and PWD methods are closer to the theoretical PSF at a high frequency while an obvious under-sampling issue can be observed in the low frequency part. SH is applied with a subharmonic order of 3 and sample level of 4. The present of SH significantly improves the performance of DFT and PWD methods in the high frequency region (with small values of r). The PSF results obtained based on SS and SU methods are very close to the theoretical values when r is less than 0.2.

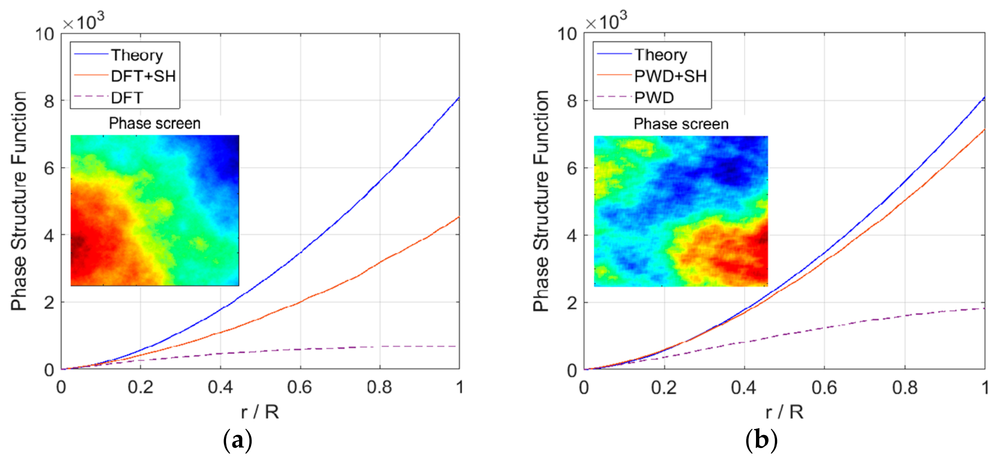

Figure 2. *Cont.*

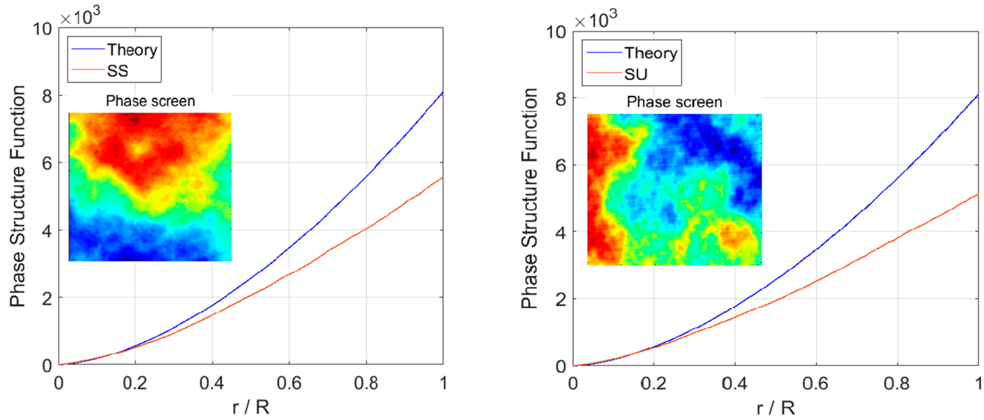

Figure 2. The generated phase screens and phase structure functions (PSFs) based on (**a**) DFT–SH method, (**b**) PWD–SH method, (**c**) SS method and (**d**) SU method. The theoretical PSF is also plotted based on Equation (9). Number of sampling points is 1024 × 1024, dimension of phase screens is 1 × 1 m and the radius R of the inscribed circle is 0.5m, according to oceanic parameters: $\eta = 0.005$ m, $\varepsilon = 10^{-4}$ m^2/s^3, $\chi_T = 10^{-7}$ K^2/s, $\omega = -0.3$.

The computational time of DFT, PWD, SS and SU methods is relatively short, and there is no significant difference between them at the sampling points from 1 to 4096 [41], so additional comparison of their computational times is not included in this paper.

To summarize, this result verified the feasibility of SS, PWD, SU methods for the phase screen generation in the high frequency region. However, the low frequency components of the phase screens generated by these methods are insufficient.

3.2. Ocean Turbulence Phase Screens Generated by SDM Based on Zernike Polynomial Method

PSFs of oceanic turbulence phase screen based on the Zernike method with different orders are studied, as shown in Figure 3. The PSF of the phase screen generated by the lower order of Zernike polynomials deviates greatly from the theoretical curve, and it is closer to the theoretical PSF with the increased order. The PSF of the phase screen exhibits a greater proximity to the theoretical curve with the growth of the order of Zernike polynomials. It can also be seen that the simulated PSF of the Zernike phase screen deviates much from the theoretical values in the high frequency region but is closer to the theoretical values at low frequency. In addition, under the same conditions, the PSFs show unusual fluctuations near the low frequency, which results in deviations from the theoretical curves because of the weakness of turbulence near the edge [31].

The insets in Figure 3 show that components simulated by order 100 Zernike are obviously sufficient than those simulated by order 10 Zernike. Moreover, since the Zernike polynomials are a group of polynomials defined on the unit circle, the phase screen is only effective in the inscribed circle area.

Although the simulation performance can be improved by increasing the order of Zernike polynomials, it can be observed that the high frequency components are still insufficient. Meanwhile, with the order of Zernike polynomials increasing, the complexity of computation increases exponentially but the improvement becomes less significant.

The computational time can intuitively reveal the simulation complexity of Zernike polynomials phase screens of different orders [32]. Therefore, the calculation time of single Zernike phase screens with the order of 10, 20, 30, 40, 50, 100 and 150 is recorded in Figure 4 separately, where the computational time of a single-phase screen generation is the average of 2000 random results.

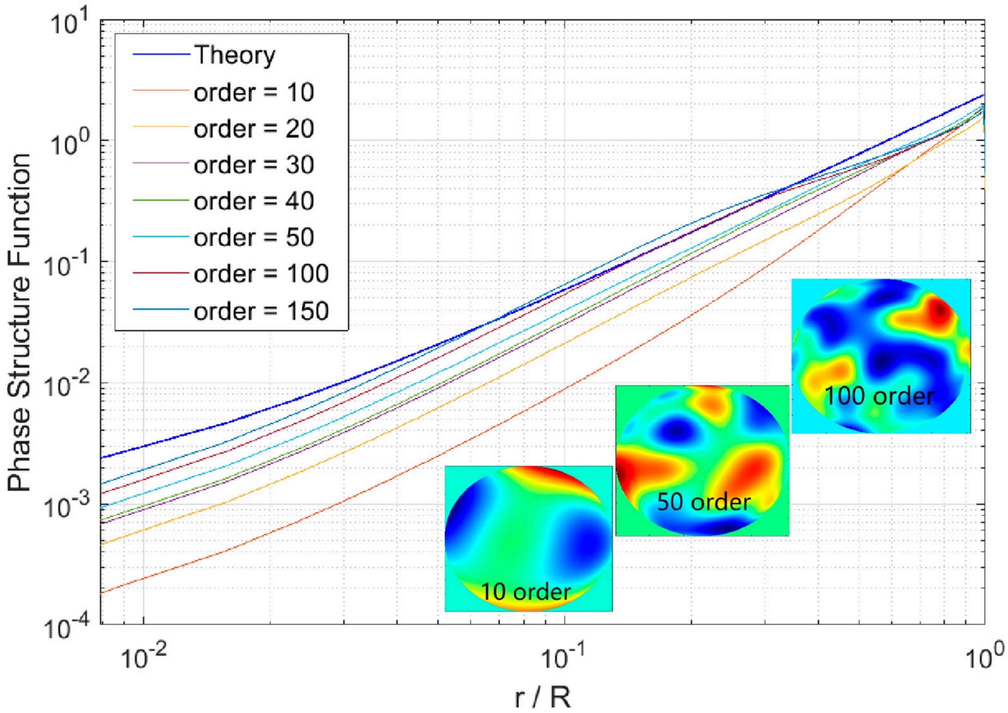

Figure 3. PSF of random phase screens obtained by different order Zernike polynomials. The insets show example phase screens generated with 10, 50, 100-order Zernike polynomials method, respectively. Number of sampling points is 1024 × 1024 and the radius R of the inscribed circle is 1 m, according to the oceanic parameters: $\eta = 0.005$ m, $\varepsilon = 10^{-4}$ m^2/s^3, $\chi_T = 10^{-7}$ K^2/s, $\omega = -0.3$.

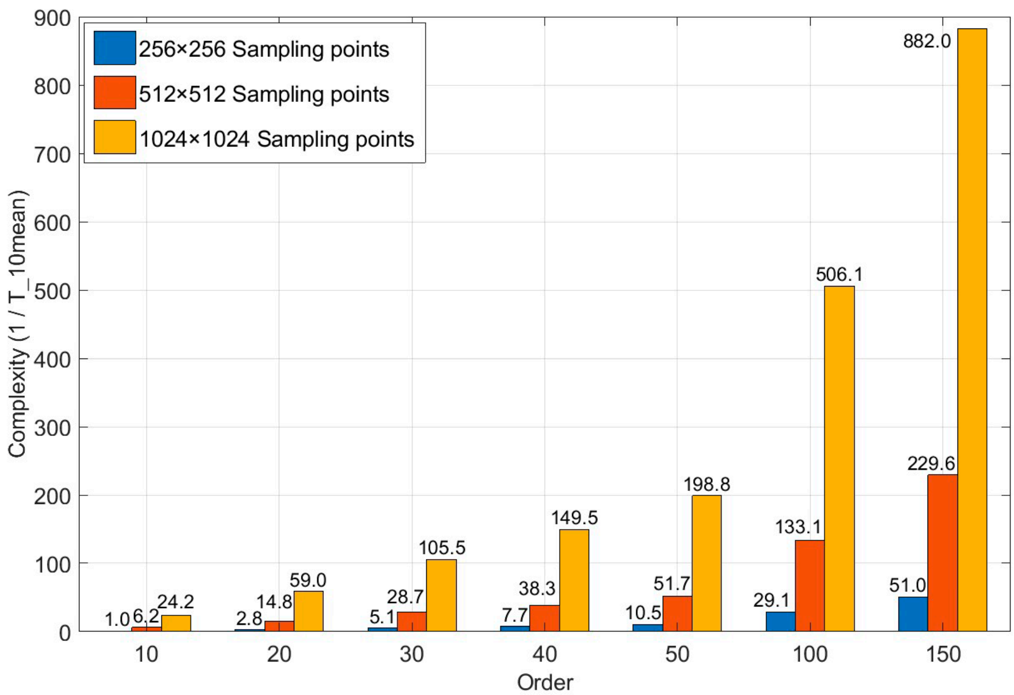

Figure 4. Complexity of Zernike phase screens with increasing order under different sampling points. Sampling points are 256 × 256, 512 × 512, 1024 × 1024, respectively.

As shown in Figure 4, all the computational times are normalized to the average computational time of the phase screen, with 256 × 256 sampling points generated by 10-order Zernike polynomials for comparison. The computational complexity increases with the order of Zernike polynomials. For 256 × 256 sampling points, the computational complexity of 20-order Zernike phase screens is only 2.8 times that of 10-order ones, while the computational complexity of order 150 became 51 times, surprisingly. For higher-order Zernike phase screens, the computational time can be extended to be on the order of hours, which is considered to be extremely inefficient and less necessary. Meanwhile, the influence of sampling points on computational complexity is also revealed. The more the sampling points are, the larger the proportion of computing time it occupies.

To summarize, to solve the issue of the Zernike phase screen with insufficient high frequency components, the order of Zernike polynomials can be continuously increased but there is always a trade-off between the performance and computational efficiency.

3.3. Ocean Turbulence Phase Screens Generated by Hybrid Methods

In this section, four hybrid methods based on FSM and SDM are investigated (i.e., DFT + Zernike, PWD + Zernike, SS + Zernike and SU + Zernike methods). The PSFs of the phase screens generated by these methods are plotted in Figure 5 with the optimization of superposition coefficients. The 50-order Zernike phase screens are selected in this simulation as a trade-off of its relatively reasonable accuracy and computational complexity. The insets in Figure 5 show the examples of hybrid phase screens, which only consider the effective area of the inscribed circle.

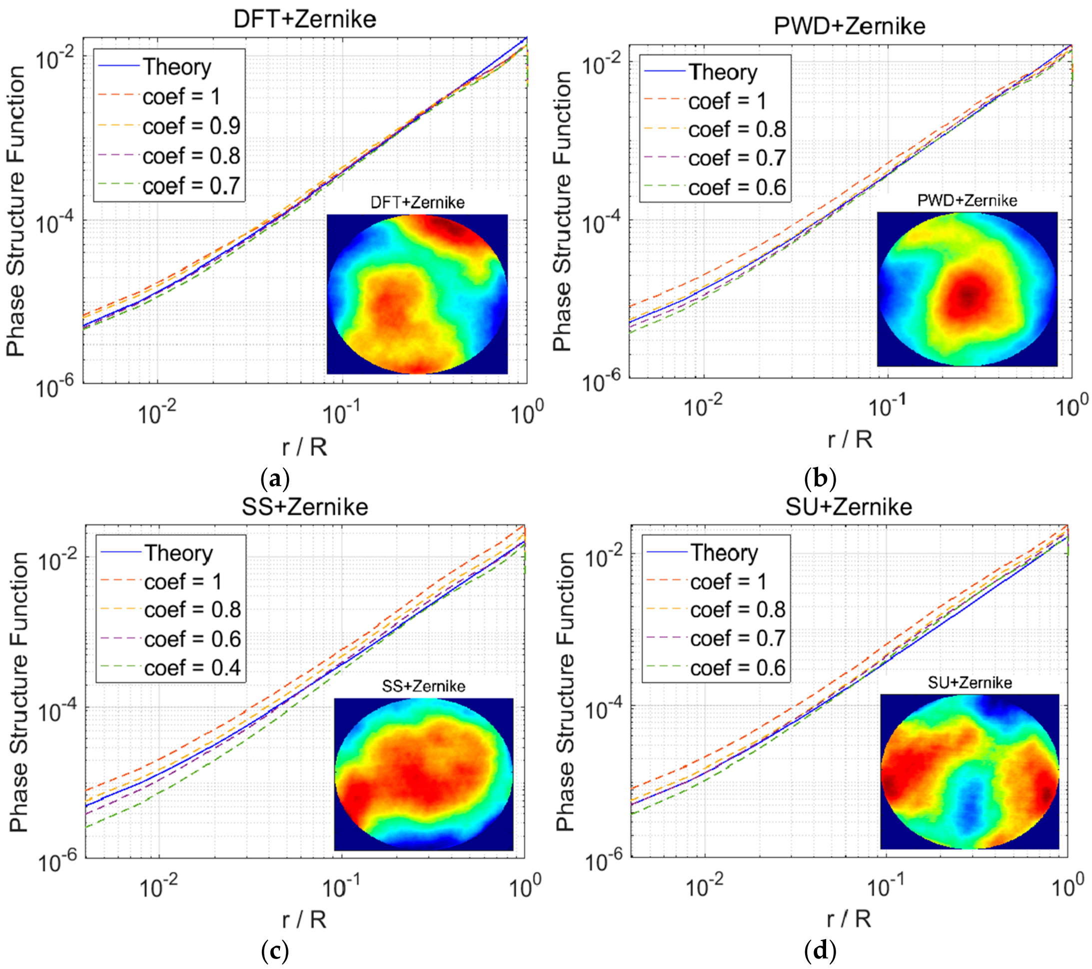

Figure 5. Comparison of PSF of hybrid phase screen methods with theoretical values under different superposition coefficients and phase screen examples. All four methods are (**a**) the DFT + Zernike hybrid method, (**b**) the PWD + Zernike hybrid method, (**c**) the SS + Zernike hybrid method and (**d**) the SU + Zernike hybrid method. Sampling points are 1024 × 1024, the radius R of the inscribed circle is 5cm and relative oceanic parameters: $\eta = 0.0001$ m, $\varepsilon = 0.01\ \mathrm{m}^2/\mathrm{s}^3$, $\chi_T = 10^{-10}\ \mathrm{K}^2/\mathrm{s}$, $\omega = -4$.

Compared with FSM or SDM, the hybrid method generates phase screens with better PSF curves and complements the insufficient frequency components. The simulation error can be mitigated by optimizing the superposition coefficients.

The optimal superposition coefficient for each hybrid method can be determined by calculating the mean square error (MSE) between the theoretical values and simulated values, as shown in Table 2. Apart from the data calculated in Table 2, the MSE of the 50-order Zernike phase screen is 20.00×10^{-3}, and that of the 100-order Zernike is 9.70×10^{-3}. Compared with the optimal error of hybrid phase screens in Table 2, it also proves that the performance of hybrid methods is superior to high-order Zernike methods. SS and 50-order Zernike show the minimum error when the superposition coefficient is 0.6.

Table 2. Error evaluation of different methods with corresponding coefficients.

		Different Superposition Coefficient MSE Error (10^{-3})				**Optimal Coef. Error**
DFT + Zernike 50	Coef.	1	0.9	0.8	0.7	**0.8**
	Error	4.43	7.27	4.17	7.49	**4.17**
SS + Zernike 50	Coef.	1	0.8	0.6	0.4	**0.6**
	Error	46.52	9.46	1.90	6.95	**1.90**
PWD + Zernike 50	Coef.	1	0.8	0.7	0.6	**0.8**
	Error	7.33	2.78	3.97	5.72	**2.78**
SU + Zernike 50	Coef.	1	0.8	0.7	0.6	**0.6**
	Error	36.72	11.09	4.55	2.80	**2.80**

In addition, the computational speed of the hybrid method has been also investigated; the time required to calculate a phase screen at different sampling points is recorded in Table 3, using the 100-order Zernike phase screen as a comparison. The computational time of hybrid methods is dominated by the Zernike method. The selected linear superposition coefficients do not change the computational time, so they are neglected in this study. The oceanic turbulence coherence length $r_0 = 0.8923$ according to the relative parameters: $\eta = 0.0001$ m, $\varepsilon = 0.01$ m^2/s^3, $\chi_T = 10^{-10}$ K^2/s, $\omega = -4$.

According to the Table 3, the computational time for the single-phase screen (one frame) at four different number of sampling points are recorded, including 256×256, 512×512, 1024×1024 and 2048×2048. The computational times of the phase screen generation of the four hybrid methods are similar to each other and all of them are shorter than that of the 100-order Zernike. In addition, the more the sampling points can result in a greater difference in computational time between the Zernike method and the hybrid methods. All methods offer a computational time of less than 1 s at the sampling points of 256×256, while the Zernike method takes half a minute longer than the hybrid methods at sampling points of 2048×2048. From [41] and Figure 4, the time used for phase screen generation by FSMs is relatively short. Therefore, the main reason for the increased computational time is the increased order of Zernike polynomials. In addition, it can be expected that the hybrid method can save much more time compared to the high-order Zernike method during the multiple phase screen generation with a large number of sampling points.

Table 3. Average computational time for one phase screen generation.

Method \ Sampling Points	Computational Time (s/Frame)			
	256 × 256	**512 × 512**	**1024 × 1024**	**2048 × 2048**
Zernike 100	0.74	3.59	15.32	52.73
DFT + Zernike 50	0.28	1.39	5.41	21.35
SS + Zernike 50	0.30	1.39	5.50	21.63
PWD + Zernike 50	0.30	1.48	5.64	21.97
SU + Zernike 50	0.30	1.37	5.40	21.32

To sum up, with an appropriate superposition coefficient, the SS + Zernike method offers better performance among the four hybrid methods, based on the results shown in this section. In the next section, this method is selected for the simulation of the optical beam propagation in oceanic turbulence.

3.4. Beam Propagation Simulation

Based on the SS + Zernike hybrid phase screen and split-step method, the simulation can be carried out to study the influence of different-level underwater turbulence on optical beam propagation. A Gaussian beam with the 3-dB beam size of 2 cm emitted from the transmission plane propagates through the underwater turbulence with a 10 m distance in z direction. The simulated impact of the oceanic turbulence on this beam was represented in 10 equally distributed SS + Zernike phase screens with the size of a 10 × 10 cm plane. In this simulation, absorption and scattering effects are not considered.

Figure 6 illustrates the phase screens generated by the SS + Zernike methods with different turbulence conditions and the simulated light spots at the receiving end. Different conditions have a different strength of turbulence according to [58], where condition 3 has the strongest strength of the turbulence effect. Figure 6a,d illustrate the simulation results under the turbulence condition 1, where $\eta = 0.0032$ m, $\varepsilon = 0.01$ m^2/s^3; $\chi_T = 10^{-8}$ K^2/s, $\omega = -0.5$; Figure 6b,e correspond to the turbulence condition 2, with $\eta = 0.0032$, $\varepsilon = 0.01$ m^2/s^3, $\chi_T = 10^{-6}$ K^2/s; $\omega = -0.5$; Figure 6c,f are produced by the turbulence condition 3, where $\eta = 0.0032$ m, $\varepsilon = 0.01$ m^2/s^3, $\chi_T = 10^{-5}$ K^2/s, $\omega = -0.5$. It can be observed that, propagating through a weak turbulence, the phase of the beam is less affected, so its power distribution is barely distorted, as shown in Figure 6d. On the other hand, the phase and intensity of the propagating beam is seriously distorted by a strong turbulence, as shown in Figure 6f.

In conclusion, we demonstrate the feasibility of using the proposed method in the simulation of the oceanic turbulence effect on light propagating in underwater. The spatial intensity and phase distributions at the receiving end can be further employed in the study and prediction of the performance degradation of practical underwater optical communication systems in a specific turbulent condition.

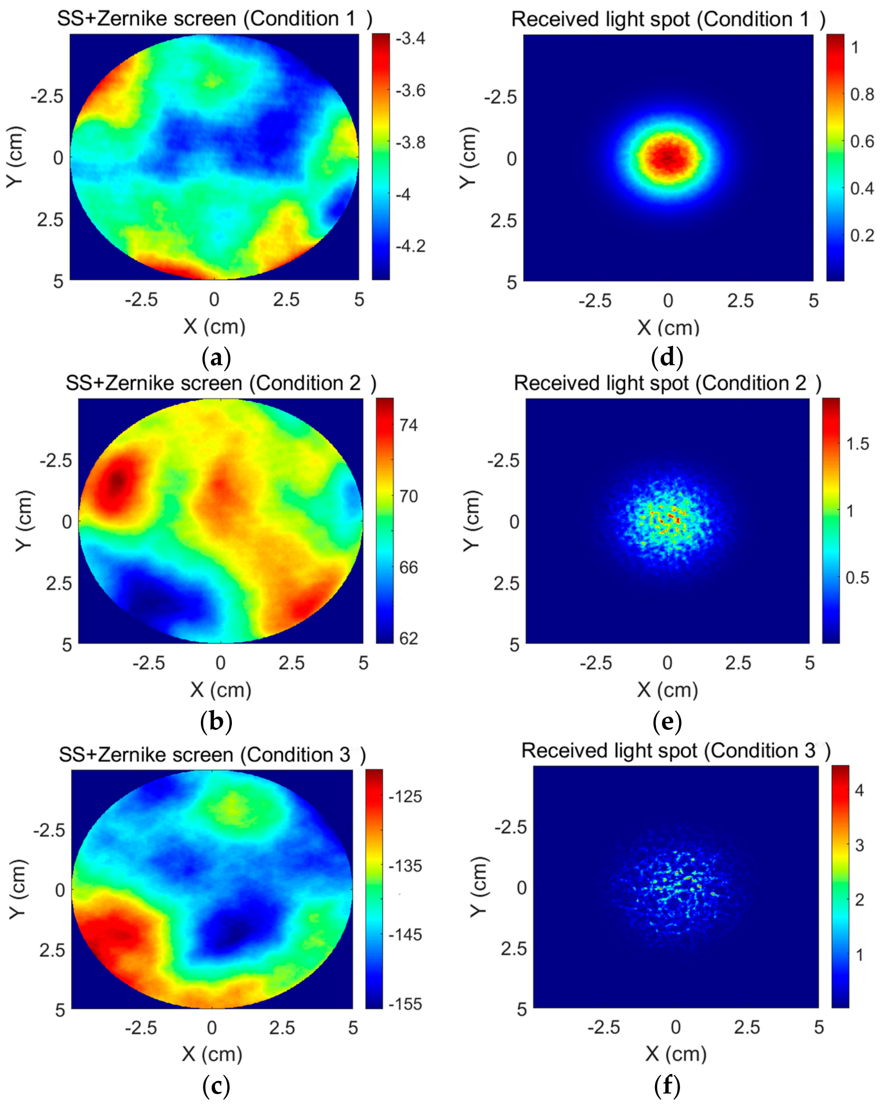

Figure 6. Light spots simulation results under different turbulence conditions using SS + Zernike hybrid phase screen. (**a**–**c**) are the corresponding SS + Zernike hybrid phase screens under conditions 1, 2, 3, respectively; (**d**–**f**) are the corresponding light spots at receiving end under conditions 1, 2, 3, respectively. Color bars in (**a**–**c**) represent phase in radian, color bars in (**b**–**f**) represent light intensities.

4. Conclusions

This paper summarized FSMs, including DFT, PWD, SS, and SU methods, which were commonly used for atmospheric turbulence. PWD, SS, and SU methods are applied to underwater turbulent environment in this work by the use of the fluctuation spectrum of ocean refractive index. The phase screens are generated based on these methods and verified by the corresponding PSFs. Meanwhile, the Zernike polynomials method of SDM is also studied with the PSF of the generated phase screen and the computational complexity.

The lack of high/low frequency components of phase screens generated by the above methods can be solved by employing the hybrid methods. Inspired by [25,32], SS + Zernike, PWD + Zernike and SU + Zernike hybrid methods are proposed and comprehensively studied in this work. They are verified to generate phase screens with better efficiency and accuracy than FSM or the Zernike method. The SS + Zernike hybrid method shows the best performance with a proper superposition coefficient. In addition, the feasibility of this method is validated by the simulation of Gaussian beam propagation in oceanic turbulence.

Our future investigations will include further improvements on the hybrid phase screen model, considering other candidates such as the fractal method and covariance method [59,60]. The investigations on the performance of UWOC systems under different turbulence conditions based on the intensity fluctuation of received light spots and the scintillation index obtained by the proposed method, will also be a part of our future work. In addition, possible approaches to mitigate the turbulence impact can be investigated.

Author Contributions: Conceptualization, X.W. and X.T.; methodology, X.W. and X.T.; software, R.J. and K.W.; writing—original draft preparation, R.J.; writing—review and editing, K.W., X.T. and X.W.; supervision, X.W. and X.T.; funding acquisition, X.W. and X.T. All authors have read and agreed to the published version of the manuscript.

Funding: The research was supported by the Engineering and Physical Sciences Research Council (EP/R026173/1, EP/T001011/1), the Royal Society (IEC\NSFC\211242), and National Natural Science Foundation of China (62201303).

Institutional Review Board Statement: Not applicable.

Informed Consent Statement: Not applicable.

Data Availability Statement: Data may be obtained from the authors upon request.

Acknowledgments: R.J. would like to express gratitude to Furong Yang of Heriot Watt University for the discussion.

Conflicts of Interest: The authors declare no conflict of interest.

References

1. Zeng, Z.; Fu, S.; Zhang, H.; Dong, Y.; Cheng, J. A survey of underwater optical wireless communications. *IEEE Commun. Surv. Tutor.* **2016**, *19*, 204–238. [CrossRef]
2. Fascista, A. Toward integrated large-scale environmental monitoring using WSN/UAV/Crowdsensing: A review of applications, signal processing, and future perspectives. *Sensors* **2022**, *22*, 1824. [CrossRef] [PubMed]
3. Islam, K.Y.; Ahmad, I.; Habibi, D.; Waqar, A. A survey on energy efficiency in underwater wireless communications. *J. Netw. Comput. Appl.* **2022**, *198*, 103295. [CrossRef]
4. Kaushal, H.; Kaddoum, G. Underwater optical wireless communication. *IEEE Access* **2016**, *4*, 1518–1547. [CrossRef]
5. Liu, L.; Zhou, S.; Cui, J. Prospects and problems of wireless communication for underwater sensor networks. *Wirel. Commun. Mob. Comput.* **2008**, *8*, 977–994.
6. Akyildiz, I.F.; Pompili, D.; Melodia, T. Challenges for efficient communication in underwater acoustic sensor networks. *ACM Sigbed Rev.* **2004**, *1*, 3–8. [CrossRef]
7. Pompili, D.; Akyildiz, I.F. Overview of networking protocols for underwater wireless communications. *IEEE Commun. Mag.* **2009**, *47*, 97–102. [CrossRef]
8. Johnson, L.J.; Jasman, F.; Green, R.J.; Leeson, M.S. Recent advances in underwater optical wireless communications. *Underw. Technol.* **2014**, *32*, 167–175. [CrossRef]
9. Duntley, S.Q. Light in the sea. *JOSA* **1963**, *53*, 214–233. [CrossRef]
10. Sun, X.; Kang, C.H.; Kong, M.; Alkhazragi, O.; Guo, Y.; Ouhssain, M.; Weng, Y.; Jones, B.H.; Ng, T.K.; Ooi, B.S. A review on practical considerations and solutions in underwater wireless optical communication. *J. Light. Technol.* **2020**, *38*, 421–431. [CrossRef]
11. Chen, H.; Chen, X.; Lu, J.; Liu, X.; Shi, J.; Zheng, L.; Liu, R.; Zhou, X.; Tian, P. Toward long-distance underwater wireless optical communication based on a high-sensitivity single photon avalanche diode. *IEEE Photonics J.* **2020**, *12*, 7902510. [CrossRef]
12. Zhu, S.; Chen, X.; Liu, X.; Zhang, G.; Tian, P. Recent progress in and perspectives of underwater wireless optical communication. *Prog. Quantum Electron.* **2020**, *73*, 100274. [CrossRef]
13. Li, C.-Y.; Huang, X.-H.; Lu, H.-H.; Huang, Y.-C.; Huang, Q.-P.; Tu, S.-C. A WDM PAM4 FSO–UWOC integrated system with a channel capacity of 100 Gb/s. *J. Light. Technol.* **2020**, *38*, 1766–1776. [CrossRef]
14. Li, C.-Y.; Lu, H.-H.; Tsai, W.-S.; Cheng, M.-T.; Ho, C.-M.; Wang, Y.-C.; Yang, Z.-Y.; Chen, D.-Y. 16 Gb/s PAM4 UWOC system based on 488-nm LD with light injection and optoelectronic feedback techniques. *Opt. Express* **2017**, *25*, 11598–11605. [CrossRef] [PubMed]
15. Zhang, J.; Kou, L.; Yang, Y.; He, F.; Duan, Z. Monte-Carlo-based optical wireless underwater channel modeling with oceanic turbulence. *Opt. Commun.* **2020**, *475*, 126214. [CrossRef]
16. Jamali, M.V.; Mirani, A.; Parsay, A.; Aboihassani, B.; Nabavi, P.; Chizari, A.; Khorramshahi, P.; Abdollahramezani, S.; Salehi, J.A. Statistical studies of fading in underwater wireless optical channels in the presence of air bubble, temperature, and salinity random variations. *IEEE Trans. Commun.* **2018**, *66*, 4706–4723. [CrossRef]
17. He, F.T.; Du, Y.; Zhang, J.L.; Fang, W.; Li, B.L.; Zhu, Y.Z. Bit error rate of pulse position modulation wireless optical communication in gamma-gamma oceanic anisotropic turbulence. *Acta Phys. Sin.* **2019**, *68*, 164206. [CrossRef]

18. Hanson, F.; Lasher, M. Effects of underwater turbulence on laser beam propagation and coupling into single-mode optical fiber. *Appl. Opt.* **2010**, *49*, 3224–3230. [CrossRef]
19. Weng, Y.; Guo, Y.; Alkhazragi, O.; Ng, T.K.; Guo, J.H.; Ooi, B.S. Impact of turbulent-flow-induced scintillation on deep-ocean wireless optical communication. *J. Light. Technol.* **2019**, *37*, 5083–5090. [CrossRef]
20. Ata, Y.; Baykal, Y. Scintillations of optical plane and spherical waves in underwater turbulence. *JOSA A* **2014**, *31*, 1552–1556. [CrossRef]
21. Dai, L.; Tong, S.; Zhang, L.; Wang, Y. On simulation and verification of the atmospheric turbulent phase screen with Zernike polynomials. In *Selected Papers from Conferences of the Photoelectronic Technology Committee of the Chinese Society of Astronautics 2014, Part II*; SPIE: Bellingham, WA, USA, 2014; pp. 372–379.
22. Frehlich, R. Simulation of laser propagation in a turbulent atmosphere. *Appl. Opt.* **2000**, *39*, 393–397. [CrossRef]
23. Moin, P.; Mahesh, K. Direct numerical simulation: A tool in turbulence research. *Annu. Rev. Fluid Mech.* **1998**, *30*, 539–578. [CrossRef]
24. Vetelino, F.S.; Young, C.; Andrews, L.; Recolons, J. Aperture averaging effects on the probability density of irradiance fluctuations in moderate-to-strong turbulence. *Appl. Opt.* **2007**, *46*, 2099–2108. [CrossRef] [PubMed]
25. Zhu, L.; Li, Y.; Zheng, D.H.; Wu, J. Performance comparison of subharnomic and Zernike polynomials method for compensation of low-frequency components in FFT-based Von Karman phase screen. In Proceedings of the 2015 International Conference on Wireless Communications & Signal Processing (WCSP), Nanjing, China, 15–17 October 2015; pp. 1–5.
26. Tang, X.; Kumar, R.; Sun, C.; Zhang, L.; Chen, Z.; Jiang, R.; Wang, H.; Zhang, A. Towards underwater coherent optical wireless communications using a simplified detection scheme. *Opt. Express* **2021**, *29*, 19340–19351. [CrossRef]
27. Mudge, K.A.; Silva, K.D.; Clare, B.A.; Grant, K.J.; Nener, B.D. Scintillation index of the free space optical channel: Phase screen modelling and experimental results. In Proceedings of the 2011 International Conference on Space Optical Systems and Applications (ICSOS), Santa Monica, CA, USA, 11–13 May 2011; pp. 403–409.
28. Zhao, S.; Yang, H.; Li, Y.; Cao, F.; Sheng, Y.; Cheng, W.; Gong, L. The influence of atmospheric turbulence on holographic ghost imaging using orbital angular momentum entanglement: Simulation and experimental studies. *Opt. Commun.* **2013**, *294*, 223–228. [CrossRef]
29. Nootz, G.; Matt, S.; Kanaev, A.; Judd, K.P.; Hou, W. Experimental and numerical study of underwater beam propagation in a Rayleigh–Bénard turbulence tank. *Appl. Opt.* **2017**, *56*, 6065–6072. [CrossRef]
30. Yang, T.; Zhao, S. Random Phase Screen Model of Ocean Turbulence. *Acta Opt. Sin.* **2017**, *37*, 1201001.
31. Roddier, N.A. Atmospheric wavefront simulation using Zernike polynomials. *Opt. Eng.* **1990**, *29*, 1174–1180. [CrossRef]
32. Zhang, B.; Qin, S.; Wang, X. Accurate and fast simulation of Kolmogorov phase screen by combining spectral method with Zernike polynomials method. *Chin. Opt. Lett.* **2010**, *8*, 969–971.
33. Yu, N.; Genevet, P.; Kats, M.A.; Aieta, F.; Tetienne, J.-P.; Capasso, F.; Gaburro, Z. Light propagation with phase discontinuities: Generalized laws of reflection and refraction. *Science* **2011**, *334*, 333–337. [CrossRef]
34. Lu, W.; Liu, L.; Sun, J. Influence of temperature and salinity fluctuations on propagation behaviour of partially coherent beams in oceanic turbulence. *J. Opt. A Pure Appl. Opt.* **2006**, *8*, 1052–1058. [CrossRef]
35. Zhang, W.; Gao, J.; Zhang, D.; He, Y.; Xu, T.; Fickler, R.; Chen, L. Free-space remote sensing of rotation at the photon-counting level. *Phys. Rev. Appl.* **2018**, *10*, 044014. [CrossRef]
36. Zhao, S.; Leach, J.; Gong, L.; Ding, J.; Zheng, B. Aberration corrections for free-space optical communications in atmosphere turbulence using orbital angular momentum states. *Opt. Express* **2012**, *20*, 452–461. [CrossRef]
37. Fleck, J.A.; Morris, J.; Feit, M. Time-dependent propagation of high energy laser beams through the atmosphere. *Appl. Phys.* **1976**, *10*, 129–160. [CrossRef]
38. Martin, J.; Flatté, S.M. Intensity images and statistics from numerical simulation of wave propagation in 3-D random media. *Appl. Opt.* **1988**, *27*, 2111–2126. [CrossRef] [PubMed]
39. Wang, L.; Li, Q.; Wei, H.; Liao, S.; Shen, M. Numerical simulation and validation of phase screen distorted by atmospheric turbulence. *Opto-Electron. Eng.* **2007**, *34*, 1–4.
40. McGlamery, B.L. Restoration of turbulence-degraded images. *JOSA* **1967**, *57*, 293–297. [CrossRef]
41. Charnotskii, M. Four methods for generation of turbulent phase screens: Comparison. *arXiv* **2019**, arXiv:1911.09185.
42. Charnotskii, M. Sparse spectrum model for a turbulent phase. *JOSA A* **2013**, *30*, 479–488. [CrossRef]
43. Charnotskii, M. Statistics of the sparse spectrum turbulent phase. *JOSA A* **2013**, *30*, 2455–2465. [CrossRef]
44. McGlamery, B.L. Computer simulation studies of compensation of turbulence degraded images. In Proceedings of the Image Processing, Pacific Grove, CA, USA, 24–26 February 1976; pp. 225–233.
45. Paulson, D.A.; Wu, C.; Davis, C.C. Randomized spectral sampling for efficient simulation of laser propagation through optical turbulence. *JOSA B* **2019**, *36*, 3249–3262. [CrossRef]
46. Pan, S.; Wang, L.; Wang, W.; Zhao, S. An effective way for simulating oceanic turbulence channel on the beam carrying orbital angular momentum. *Sci. Rep.* **2019**, *9*, 14009. [CrossRef]
47. Nikishov, V.V.; Nikishov, V.I. Spectrum of turbulent fluctuations of the sea-water refraction index. *Int. J. Fluid Mech. Res.* **2000**, *27*, 82–98. [CrossRef]
48. Lu, L.; Ji, X.; Baykal, Y. Wave structure function and spatial coherence radius of plane and spherical waves propagating through oceanic turbulence. *Opt. Express* **2014**, *22*, 27112–27122. [CrossRef]

49. Hill, R.J. Optical propagation in turbulent water. *JOSA* **1978**, *68*, 1067–1072. [CrossRef]
50. Cheng, Y.; Canuto, V.M. Stably stratified shear turbulence: A new model for the energy dissipation length scale. *J. Atmos. Sci.* **1994**, *51*, 2384–2396. [CrossRef]
51. Gargett, A.E.; Holloway, G. Sensitivity of the GFDL ocean model to different diffusivities for heat and salt. *J. Phys. Oceanogr.* **1992**, *22*, 1158–1177. [CrossRef]
52. Carbillet, M.; Riccardi, A. Numerical modeling of atmospherically perturbed phase screens: New solutions for classical fast Fourier transform and Zernike methods. *Appl. Opt.* **2010**, *49*, G47–G52. [CrossRef]
53. Noll, R.J. Zernike polynomials and atmospheric turbulence. *JOSA* **1976**, *66*, 207–211. [CrossRef]
54. Roddier, N.A. *Curvature Sensing for Adaptive Optics: A Computer Simulation*; The University of Arizona: Tucson, AZ, USA, 1989.
55. Pan, S. Research on Random Phase Screen Model for Simulating Underwater Turbulence. Master's Thesis, Nanjing University of Posts and Telecommunications, Nanjing, China, 2020. (In Chinese).
56. Zhai, H.; Wang, B.; Zhang, J.; Dang, A. Fractal phase screen generation algorithm for atmospheric turbulence. *Appl. Optics* **2015**, *54*, 4023–4032. [CrossRef]
57. Lane, R.G.; Glindemann, A.; Dainty, J.C. Simulation of a Kolmogorov phase screen. *Waves Random Media* **1992**, *2*, 209–224. [CrossRef]
58. Gökçe, M.C.; Baykal, Y. Aperture averaging in strong oceanic turbulence. *Opt. Commun.* **2018**, *413*, 196–199. [CrossRef]
59. Wallner, E.P. Optimal wave-front correction using slope measurements. *JOSA* **1983**, *73*, 1771–1776. [CrossRef]
60. Mandelbrot, B.B. *Multifractals and 1/f Noise: Wild Self-Affinity in Physics (1963–1976)*; Springer: New York, NY, USA, 1999.